Magnetic dual-layer equivalent sources on the sphere

Arthur Siqueira-Macedo[1], Leonardo Uieda[1], India Uppal[2]

[1] Universidade de São Paulo, Brazil; [2] University of Liverpool, UK;

Corresponding author: Arthur Siqueira-Macedo <arthursmacedo@usp.br>

Received in original form on 2026/03/10.

Disclaimer:

This is a peer-reviewed author-produced postprint of the article "Siqueira-Macedo *et al.* (2026). Magnetic dual-layer equivalent sources on the sphere. *Journal of Geophysical Research: Solid Earth*. doi:10.1029/2026JB034259". The postprint is available from EarthArXiv at https://doi.org/10.31223/X5M19R.

Open research: The source code used to generate all of the results presented in this research can be freely accessed and reused under the terms of an open license. You can find it at https://doi.org/10.5281/zenodo.18509844 and https://github.com/compgeolab/eqs-magnetic-spherical.

© 2026 The Authors. Available under the Creative Commons Attribution 4.0 International License.

Plain language summary

Mapping the Earth's magnetic field using airplanes is a common technique, but traditional modeling and gridding methods process this data as if the Earth were flat. Because our planet is round, projecting this information onto a flat surface introduces distortions, causing mapping errors over large areas. In this study, we updated the math behind these calculations to account for the Earth's actual curvature, allowing for accurate magnetic maps on a regional or global scale. To improve the results, we used a "dual-layer" model that captures both deep, broad magnetic features and shallow, detailed ones. Because mapping large areas involves massive amounts of data, we also added an advanced computational technique that allows computers to process the information much faster. We successfully tested our new method on over 1.5 million real observations, proving it is fast, reliable, and highly useful for understanding the geology of large regions. Finally, we released our software for free as open-source so anyone can use it.

Abstract

The equivalent source method is widely used for processing and interpolating magnetic data, particularly in airborne surveys. However, implementations based on Cartesian coordinates present limitations at regional and global scales, where Earth curvature introduces geometric inconsistencies that affect data integration and modeling accuracy. To address this problem, this study proposes an adaptation of the magnetic equivalent source method to spherical coordinates, including revisions to its mathematical formulation to account for spherical geometry. The proposed framework enables consistent magnetic field modeling over large geographic areas. To improve the representation of magnetic sources, a dual-layer configuration is adopted to separate long- and short-wavelength components. Cross-validation is employed to determine optimal hyperparameters for each layer, ensuring stable and balanced inversions. To guarantee computational feasibility for large and high-resolution datasets, a gradient-boosting strategy is incorporated into the inversion process, significantly improving computational performance. Synthetic experiments demonstrate that the method remains stable and accurate for large-scale datasets, with tests conducted on synthetic data containing up to 500,000 observations and enables the reliable recovery of magnetic field components from total-field anomaly data. The approach was further applied to more than 1.5 million real observations, confirming its scalability and robustness. The recovered field amplitude provides additional constraints for data interpretation and enhances the geological analysis. The final implementation is released as open-source software to support reproducibility and broader adoption.

1 Introduction

Magnetic field studies play a critical role in geophysics, offering insights into the Earth's subsurface structures and geological composition. One of the techniques for processing magnetic data is the equivalent sources method, a mathematical tool based on physical principles from potential theory. The method takes advantage of the inherent ambiguity of potential fields. The method approximates observed anomalies using a layer of fictitious sources. Once the physical properties of these sources are estimated, they can be used to compute derived quantities at any location, such as data continuation (Emilia, 1973; Li et al., 2023; ZhiWen et al., 2022), gridding and interpolation (Cordell, 1992; Dampney, 1969; Ebbing et al., 2021; Li and Morozov, 2006; Mendonça and Silva, 1994, 1995), and reduction to the pole (Guspí and Novara, 2009; Li, 2001; Silva, 1986).

Although effective, the practical application of the equivalent sources technique faces a hurdle: its high computational cost. Most formulations of the equivalent sources inverse problem require the solution of dense linear systems, whose size is equal to or greater than the number of data.

Since modern airborne surveys generate large volumes of data, solving the linear systems of the equivalent-layer technique becomes demanding in terms of both processing time and memory (Oliveira Junior et al., 2023). To improve computational efficiency, several strategies have been developed. These include methods based on moving data windows (Leão and Silva, 1989; Soler and Uieda, 2021; Uppal et al., 2025), column- and row-action updates (Cordell, 1992; Guspí and Novara, 2009; Mendonça and Silva, 1994), reparametrization of the equivalent layer (Mendonça, 2020; Oliveira Jr. et al., 2013), sparsity-inducing transformations using wavelets and quadtree discretization (Barnes and Lumley, 2011; Li and Oldenburg, 2010), iterative methods using the full sensitivity matrix (Jirigalatu and Ebbing, 2019; Siqueira et al., 2017; Xia and Sprowl, 1991; Xia et al., 1993), and iterative or direct deconvolution exploiting Block-Toeplitz Toeplitz-block (BTTB) structures (Takahashi et al., 2020, 2022).

Most equivalent source approaches are formulated in Cartesian coordinates, which are well-suited for relatively small areas. To apply these methods to larger regions, data natively registered in geodetic coordinates must first be projected onto a planar surface. Although this projection intrinsically introduces distortions in distances, areas, and relative positioning, quantifying the exact impact of these distortions relative to typical survey uncertainties is an extensive task. However, the fundamental limitation of Cartesian formulations becomes absolute at the global scale, where no single map projection is adequate and periodic boundary conditions in longitude are required. Therefore, a spherical formulation of the forward and inverse problem offers a mathematically rigorous alternative. By operating directly on the curved Earth and avoiding planar projections, the spherical approach provides an exact solution that is uniquely capable of seamless modeling from regional scales to global satellite datasets.

The use of equivalent sources for modeling the Earth's magnetic field evolved through various formulations from the late 1960s to the early 1980s (Alldredge and Stearns, 1969; Mayhew et al., 1980; Mayhew, 1979, 1982; Reilly and Herbrechtsmeier, 1978). For instance, Mayhew (1979) successfully applied an equivalent source representation using arrays of dipoles and spherical prisms to model satellite magnetic anomaly data. Later, von Frese et al. (1981) developed a systematic procedure for the comprehensive geologic analysis of both gravity and magnetic anomalies in spherical coordinates. They formalized the equivalent point source inversion as a computationally efficient alternative to spherical harmonics, which become computationally challenging at high degrees, and to Fourier transforms, which require planar projection of spherical data. Their approach relates po-

tential field anomalies directly to a distribution of equivalent point sources on a sphere through least squares matrix inversion. More recently, Kother et al. (2015) extended the regularized monopole approach of O'Brien and Parker (1994) to global lithospheric field modelling using CHAMP satellite data. They placed approximately 30, 000 monopoles on an icosahedral grid 100 km below the surface and estimated their strengths through an iteratively reweighted least-squares inversion with quadratic or entropy-based regularization. This strategy provided localized and scalable representations of the lithospheric field, while preserving the ability to transform results into spherical harmonics for global comparisons.

Adopting a spherical geometry, however, presents new challenges for implementing window-based computational strategies like the gradient-boosting method of Soler and Uieda (2021) and Uppal et al. (2025). A prerequisite for such methods is the effective subdivision of the spherical surface into discrete, manageable cells for localized processing. Methods for tessellating a sphere into equal-area cells are essential for this task, as they ensure that each window contributes equally to the inversion, avoiding biases from uneven cell sizes. While various methods for spherical tessellation exist, such as those based on hierarchical grids like HEALPix (Gorski et al., 1998), they can be challenging to implement computationally. A simpler and more direct alternative is the isolatitudinal method proposed by Malkin (2016). This method divides the sphere into latitudinal bands, which are then subdivided into equal-area cells. This approach provides a straightforward way to define the processing windows required for our gradient boosting algorithm in a spherical context.

A further challenge of equivalent source models is the simultaneous modeling of magnetic signals originating from different depths, and hence which have different wavelengths. A single layer of equivalent sources often struggles to capture both short-wavelength anomalies from shallow crustal bodies and the long-wavelength regional fields from deeper sources. To address this, Li et al. (2020) introduced a dual-layer equivalent source model, with a shallow layer of rectangular prisms for local features and a deep layer of prisms for the regional field. While effective, their approach of fitting both layers simultaneously is computationally intensive and requires a depth-weighting factor to prevent the inversion from being dominated by the shallow layer. A recent refinement by Uppal et al. (2025) overcomes these issues by fitting the layers sequentially: the deep layer is fitted first to a block-averaged, long-wavelength version of the data, and the shallow layer is then fitted to the high-frequency residuals. Expanding on this sequential strategy, Heincke et al. (2026) successfully utilized three equivalent source layers that are subsequently fitted to model large-scale magnetic anomalies.

This work introduces a unified method that simultaneously addresses both the computational and geometric challenges inherent in large-scale magnetic data processing. We develop and implement a spherical equivalent source technique that integrates recent advancements from Soler and Uieda (2021) and Uppal et al. (2025). Specifically, our approach extends the gradient-boosting strategy to the sphere (Soler and Uieda, 2021) and employs a dual-layer configuration (Uppal et al., 2025) into a windowed inversion method adapted for the Earth's spherical geometry.

2 Methodology

2.1 Magnetic field of a dipole in spherical coordinates

This section details the mathematical method for computing the magnetic field vector $\vec{\mathbf{B}}$ from a magnetic dipole source, based on the classical works of von Frese et al. (1981) and Langel and Hinze (1998). The formulation requires the definition of three distinct coordinate systems. The primary ref-

erence is a geocentric Cartesian system (X, Y, Z), within which a geocentric spherical system (r, θ, λ) is used to formulate the physics (Figure 1a). However, as airborne survey data are typically provided in a geodetic system (latitude φ, longitude λ, height h), this system must also be considered. Figure 1b illustrates the geometric relationship between the geodetic and geocentric latitudes, whose difference arises from the Earth's oblateness. The practical application of the physical model to real-world data therefore necessitates transformations between these coordinate systems.

A key challenge in spherical coordinates is that the local orthonormal basis vectors $(\hat{\mathbf{r}}, \hat{\boldsymbol{\theta}}, \hat{\boldsymbol{\lambda}})$ are position-dependent (see Figure 1a). Consequently, the magnetic moment vector $\vec{\mathbf{m}}'$, defined in the local basis at the source point Q, and the magnetic field vector $\vec{\mathbf{B}}$, measured in the local basis at the observation point P, reside in different reference frames. To relate these two vectors, the source's magnetic moment must first be rotated into the observer's local coordinate system.

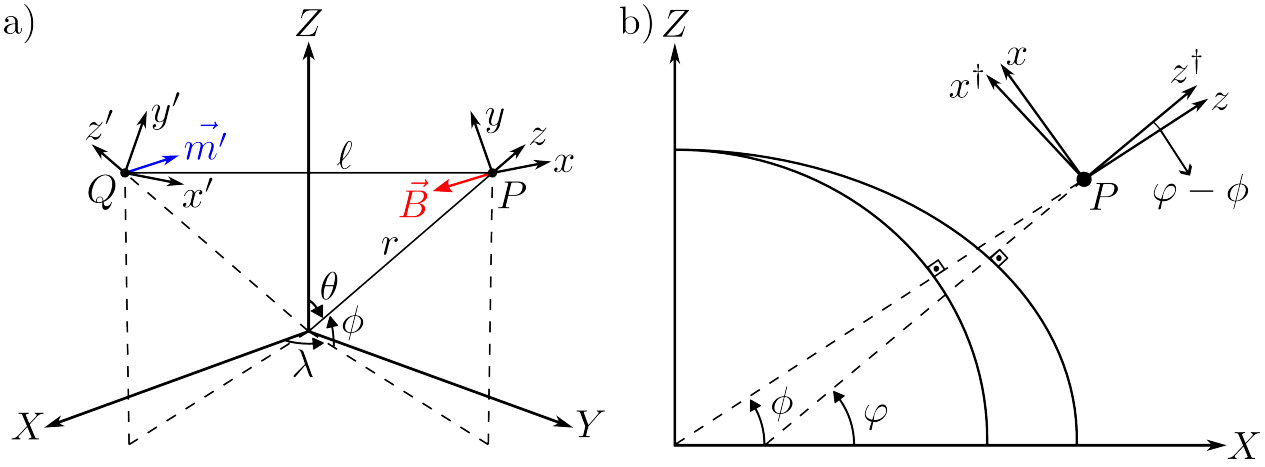


Figure 1: Geometric configuration of the magnetic dipole field calculation. **(a)** Spherical coordinate system centered at the origin, with the equivalent magnetic dipole located at point Q, characterized by its magnetic moment vector $\mathbf{m}'$ (blue). The magnetic field $\mathbf{B}$ (red) is evaluated at point P. Both locations have their respective local reference frames defined by the spherical basis vectors $(\hat{\mathbf{r}}, \hat{\boldsymbol{\theta}}, \hat{\boldsymbol{\lambda}})$. **(b)** Geodetic coordinate system illustrating the relationship between geodetic latitude φ and spherical (geocentric) latitude ϕ, which defines the rotation angle $\Delta\Phi$ needed for coordinate conversion.

This transformation is achieved through a rotation matrix, $\mathbf{R}$, which maps the components of the source moment from the basis at Q to the basis at P. The rotated magnetic moment, $\mathbf{m}$, is given by

$$\mathbf{m} = \mathbf{R}\mathbf{m}'. \tag{1}$$

The rotation matrix $\mathbf{R}$ is composed of the direction cosines between the unit vectors of the two local spherical bases

$$\mathbf{R} = \begin{bmatrix} \delta_{rr'} & \delta_{r\theta'} & \delta_{r\lambda'} \\ \delta_{\theta r'} & \delta_{\theta\theta'} & \delta_{\theta\lambda'} \\ \delta_{\lambda r'} & \delta_{\lambda\theta'} & \delta_{\lambda\lambda'} \end{bmatrix}, \tag{2}$$

where each element $\delta_{uv'}$ represents the dot product $\hat{\mathbf{u}} \cdot \hat{\mathbf{v}}'$. The expressions for these direction cosines, which depend on the coordinates of both the source and observation points, are

$$\delta_{rr'} = \cos\theta\cos\theta' + \sin\theta\sin\theta'\cos(\lambda - \lambda') \tag{3a}$$
$$\delta_{r\theta'} = -\cos\theta\sin\theta' + \sin\theta\cos\theta'\cos(\lambda - \lambda') \tag{3b}$$
$$\delta_{r\lambda'} = \sin\theta\sin(\lambda - \lambda') \tag{3c}$$
$$\delta_{\theta r'} = -\sin\theta\cos\theta' + \cos\theta\sin\theta'\cos(\lambda - \lambda') \tag{3d}$$
$$\delta_{\theta\theta'} = \sin\theta\sin\theta' + \cos\theta\cos\theta'\cos(\lambda - \lambda') \tag{3e}$$
$$\delta_{\theta\lambda'} = \cos\theta\sin(\lambda - \lambda') \tag{3f}$$
$$\delta_{\lambda r'} = -\sin\theta'\sin(\lambda - \lambda') \tag{3g}$$
$$\delta_{\lambda\theta'} = -\cos\theta'\sin(\lambda - \lambda') \tag{3h}$$
$$\delta_{\lambda\lambda'} = \cos(\lambda - \lambda'). \tag{3i}$$

Once the magnetic moment is expressed in the observer's reference frame, the magnetic field vector $\vec{\mathbf{B}}$ can be calculated. The complete relationship is a linear transformation given by

$$\vec{\mathbf{B}} = \frac{\mu_0}{4\pi}\mathbf{H}\mathbf{R}\mathbf{m}'. \tag{4}$$

Here, μ_0 is the magnetic permeability of free space, and $\mathbf{H}$ is the kernel matrix that encapsulates the physics of the dipole field in spherical coordinates. The components of $\mathbf{H}$ are functions of the radial distances (r, r') and the direction cosines, defined as

$$\mathbf{H} = \begin{bmatrix} H_{rr} & H_{r\theta} & H_{r\lambda} \\ H_{\theta r} & H_{\theta\theta} & H_{\theta\lambda} \\ H_{\lambda r} & H_{\lambda\theta} & H_{\lambda\lambda} \end{bmatrix}, \tag{5}$$

with the individual elements given by

$$H_{rr} = \frac{3(r - r'\delta_{rr'})(r\delta_{rr'} - r')}{\ell^5} - \frac{\delta_{rr'}}{\ell^3} \tag{6a}$$
$$H_{r\theta} = \frac{3(r - r'\delta_{rr'})(r\delta_{r\theta'})}{\ell^5} - \frac{\delta_{r\theta'}}{\ell^3} \tag{6b}$$
$$H_{r\lambda} = \frac{3(r - r'\delta_{rr'})(r\delta_{r\lambda'})}{\ell^5} - \frac{\delta_{r\lambda'}}{\ell^3} \tag{6c}$$
$$H_{\theta r} = -\frac{3(r'\delta_{\theta r'})(r\delta_{rr'} - r')}{\ell^5} + \frac{\delta_{\theta r'}}{\ell^3} \tag{6d}$$
$$H_{\theta\theta} = -\frac{3(r'\delta_{\theta r'})(r\delta_{r\theta'})}{\ell^5} + \frac{\delta_{\theta\theta'}}{\ell^3} \tag{6e}$$
$$H_{\theta\lambda} = -\frac{3(r'\delta_{\theta r'})(r\delta_{r\lambda'})}{\ell^5} + \frac{\delta_{\theta\lambda'}}{\ell^3} \tag{6f}$$
$$H_{\lambda r} = -\frac{3(r'\delta_{\lambda r'})(r\delta_{rr'} - r')}{\ell^5} + \frac{\delta_{\lambda r'}}{\ell^3} \tag{6g}$$
$$H_{\lambda\theta} = -\frac{3(r'\delta_{\lambda r'})(r\delta_{r\theta'})}{\ell^5} + \frac{\delta_{\lambda\theta'}}{\ell^3} \tag{6h}$$
$$H_{\lambda\lambda} = -\frac{3(r'\delta_{\lambda r'})(r\delta_{r\lambda'})}{\ell^5} + \frac{\delta_{\lambda\lambda'}}{\ell^3} \tag{6i}$$

These expressions are based on the formulation presented by Langel and Hinze (1998, see Table 5.2). However, the components $H_{\lambda r}$ and $H_{\lambda\theta}$ in Equations 6g and 6h incorporate the correction proposed by Dyment and Arkani-Hamed (1998). During our implementation, we verified that this correction is consistent with the expressions adopted in subsequent studies. In particular, a discrepancy in the direction cosines associated with these terms was identified and corrected accordingly.

In these expressions, ℓ is the Euclidean distance between the observation point P and the source point Q, which can be computed in spherical geometry as

$$\ell = \sqrt{r^2 + r'^2 - 2rr'\delta_{rr'}}. \tag{7}$$

2.1.1 Conversion between geodetic and spherical coordinates

Our implementation requires a workflow to handle the discrepancy between different coordinate systems. While the physical equations of the dipole field are formulated in a geocentric spherical system (radius r, colatitude θ, longitude λ), the input data from airborne surveys are typically provided in a geodetic system (latitude φ, longitude λ, height h). The conversion process involves two parts: converting the coordinates of the points and rotating the components of vectors. First, the geodetic coordinates of both observation points and sources are converted to their spherical equivalents using the direct, closed-form algebraic method of Vermeille (2002).

Second, vector quantities are rotated between the local reference frames. The rotation is defined by the angular difference between the geodetic (φ) and geocentric (ϕ) latitudes, $\Delta\Phi = \varphi - \phi$ (Figure 1b). As part of our workflow, the input magnetic moment vector of a source, $\vec{\mathbf{m}}$, with geodetic components $(m_{x^\dagger}, m_{y^\dagger}, m_{z^\dagger})$, is first rotated into the local spherical frame to obtain the spherical components (m_x, m_y, m_z)

$$\begin{bmatrix} m_x \\ m_y \\ m_z \end{bmatrix} = \begin{bmatrix} \cos(\Delta\Phi) & 0 & \sin(\Delta\Phi) \\ 0 & 1 & 0 \\ -\sin(\Delta\Phi) & 0 & \cos(\Delta\Phi) \end{bmatrix} \begin{bmatrix} m_{x^\dagger} \\ m_{y^\dagger} \\ m_{z^\dagger} \end{bmatrix}. \tag{8}$$

After the main physical calculation, the resulting magnetic field vector $\vec{\mathbf{B}}$, with spherical components (B_x, B_y, B_z), is rotated back into the local geodetic frame to obtain the output components $(B_{x^\dagger}, B_{y^\dagger}, B_{z^\dagger})$. This inverse transformation is achieved using the transpose of the rotation matrix

$$\begin{bmatrix} B_{x^\dagger} \\ B_{y^\dagger} \\ B_{z^\dagger} \end{bmatrix} = \begin{bmatrix} \cos(\Delta\Phi) & 0 & -\sin(\Delta\Phi) \\ 0 & 1 & 0 \\ \sin(\Delta\Phi) & 0 & \cos(\Delta\Phi) \end{bmatrix} \begin{bmatrix} B_x \\ B_y \\ B_z \end{bmatrix}. \tag{9}$$

2.2 Equivalent sources in spherical coordinates

The equivalent source technique models an observed potential field using the superposition of fields from a set of discrete sources distributed on an equivalent layer (Dampney, 1969; Oliveira Junior et al., 2023). In this work, we use this technique to model the total-field magnetic anomaly by estimating the magnetic moment magnitudes of a set of dipole sources.

Let $\mathbf{d}^o$ be the vector containing N observations of the total-field anomaly. As derived in studies

like Blakely (1995, p. 179), the total-field anomaly, ΔT, can be approximated as the projection of the anomalous magnetic field vector, $\vec{\mathbf{B}}$, onto the unit vector of the geomagnetic main field, $\hat{\mathbf{F}}$

$$\Delta T \approx \vec{\mathbf{B}} \cdot \hat{\mathbf{F}}. \tag{10}$$

The total anomalous field, $\mathbf{B}$, at any observation point is the sum of the contributions from all M equivalent sources. Therefore, the predicted total-field anomaly d_i for the i-th observation is given by the summation

$$d_i = \sum_{j=1}^{M} A_{ij} p_j, \tag{11}$$

where $p_j = \|\vec{\mathbf{m}}_j\|$ is the magnetic moment magnitude of the j-th source, and A_{ij} is the element of the sensitivity matrix. This element is defined as

$$A_{ij} = \vec{\mathbf{b}}_{ij} \cdot \hat{\mathbf{F}}, \tag{12}$$

where $\vec{\mathbf{b}}_{ij}$ is the magnetic field vector generated by the j-th source with a unit magnetic moment at the i-th observation point, as derived in the previous section in equation 4.

Writing this system of equations for all N observation points results in the matrix form

$$\begin{bmatrix} d_1 \\ d_2 \\ \vdots \\ d_N \end{bmatrix}_{N\times 1} = \begin{bmatrix} \vec{\mathbf{b}}_{11} \cdot \hat{\mathbf{F}} & \vec{\mathbf{b}}_{12} \cdot \hat{\mathbf{F}} & \cdots & \vec{\mathbf{b}}_{1M} \cdot \hat{\mathbf{F}} \\ \vec{\mathbf{b}}_{21} \cdot \hat{\mathbf{F}} & \vec{\mathbf{b}}_{22} \cdot \hat{\mathbf{F}} & \cdots & \vec{\mathbf{b}}_{2M} \cdot \hat{\mathbf{F}} \\ \vdots & \vdots & \ddots & \vdots \\ \vec{\mathbf{b}}_{N1} \cdot \hat{\mathbf{F}} & \vec{\mathbf{b}}_{N2} \cdot \hat{\mathbf{F}} & \cdots & \vec{\mathbf{b}}_{NM} \cdot \hat{\mathbf{F}} \end{bmatrix}_{N\times M} \begin{bmatrix} p_1 \\ p_2 \\ \vdots \\ p_M \end{bmatrix}_{M\times 1}. \tag{13}$$

This linear system, which constitutes the forward problem, can be expressed more compactly as

$$\mathbf{d} = \mathbf{A}\mathbf{p}. \tag{14}$$

The inverse problem consists of estimating the parameter vector $\mathbf{p}$, containing the M magnetic moment amplitudes, that best fits the observed data $\mathbf{d}^o$. Since this problem is typically ill-posed, we introduce a Tikhonov regularization term, leading to a damped least-squares formulation (Soler and Uieda, 2021). The objective function is formulated using a scaling factor as

$$\beta(\mathbf{c}) = [\mathbf{d}^o - \mathbf{U}\mathbf{c}]^\mathsf{T}\mathbf{W}[\mathbf{d}^o - \mathbf{U}\mathbf{c}] + \lambda\, \mathbf{c}^\mathsf{T}\mathbf{c}, \tag{15}$$

where $\mathbf{W}$ is a diagonal matrix of data weights, $\mathbf{U} = \mathbf{A}\mathbf{S}^{-1}$ is the scaled sensitivity matrix, $\mathbf{c} = \mathbf{S}\mathbf{p}$ is the scaled parameter vector, and λ is a dimensionless damping parameter. The scaling matrix $\mathbf{S}$ is defined as

$$\mathbf{S} = \begin{bmatrix} \sigma_1 & 0 & \cdots & 0 \\ 0 & \sigma_2 & \cdots & 0 \\ \vdots & \vdots & \ddots & \vdots \\ 0 & 0 & \cdots & \sigma_M \end{bmatrix}, \tag{16}$$

with σ_j being the standard deviation of the jth column of $\mathbf{A}$. This normalization makes the vector $\mathbf{c}$ have data units and narrows the effective search range for λ, which can typically vary between 10^{-6} and 10^{4}.

Minimizing the objective function in Equation 15 leads to the normal equations

$$(\mathbf{U}^\top \mathbf{W}\mathbf{U} + \lambda \mathbf{I})\,\hat{\mathbf{c}} = \mathbf{U}^\top \mathbf{W}\mathbf{d}^o, \tag{17}$$

whose solution gives the scaled parameters $\hat{\mathbf{c}}$. The estimated magnetic moments are then obtained by removing the scaling

$$\hat{\mathbf{p}} = \mathbf{S}^{-1}\hat{\mathbf{c}}. \tag{18}$$

Once the vector of moments $\hat{\mathbf{p}}$ is estimated, it can be used not only to reproduce the observed total-field anomaly but also to compute the full anomalous magnetic field vector $\vec{\mathbf{B}}$ and its components at any location

$$\vec{\mathbf{B}}(r, \theta, \lambda) = \sum_{j=1}^{M} \vec{\mathbf{b}}_j(r, \theta, \lambda)\, \hat{p}_j. \tag{19}$$

This capability of retrieving the vector field directly from the equivalent sources makes the method particularly powerful for multi-scale magnetic modeling (Li et al., 2020; Uppal et al., 2025).

To accurately model complex magnetic anomalies, we employ the dual-layer gradient-boosted equivalent sources method introduced by Uppal et al. (2025), illustrated in Figure 2, this methodology first fits a deep layer of equivalent sources using block-averaged or decimated data to capture the regional, long-wavelength signals. Subsequently, a shallow layer is fitted to the residuals of the deep layer to resolve the short-wavelength components. The final predicted field is then obtained by combining the contributions from both layers.

2.3 Gradient boosting on the sphere

To address the computational challenges associated with inverting large-scale datasets, we adopt the gradient-boosted equivalent sources method proposed by Soler and Uieda (2021). The primary advantage of this approach is that it avoids the construction, storage, and inversion of the full $N \times M$ sensitivity matrix. Instead, it decomposes the global inverse problem into a sequence of smaller, localized problems that are solved iteratively.

The core of the method is to reframe the solution as an additive model, where the final predicted data, $\mathbf{d}$, is built by summing the contributions from sources fitted in each of the K local windows

$$\mathbf{d} = \sum_{k=1}^{K} \mathbf{A}_k \mathbf{p}_k, \tag{20}$$

where $\mathbf{A}_k$ is the sensitivity matrix relating the sources in the k-th window to all observation points, and $\mathbf{p}_k$ is the vector of corrective source moments estimated in that window.

The implementation of a window-based method like gradient boosting in spherical coordinates requires a technique for partitioning the sphere's surface into a set of discrete windows. For the inversion to be unbiased, it is crucial that these windows have approximately equal areas, ensuring that data from different regions contribute equally to the solution. To define the windows for our algorithm, we adopt the straightforward and effective isolatitudinal method proposed by Malkin

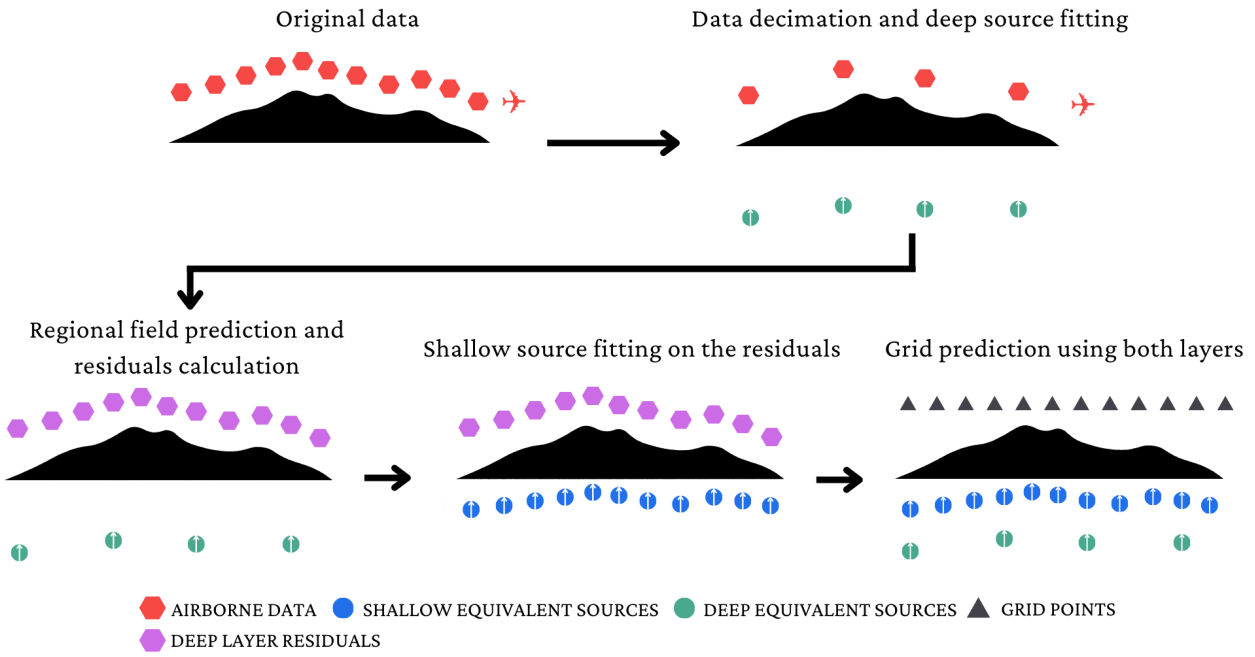


Figure 2: Flowchart of the dual-layer equivalent sources method of Uppal et al. (2025). First, the original data (red hexagons) are decimated using a blocked average procedure and then deep sources (green circles) are fitted to the decimated data. The residuals (purple hexagons) between the original data and the deep source predictions are calculated and shallow sources (blue circles) are fitted to them. Finally, the combined effect is predicted on a regular grid (black triangles) with constant height using both sets of sources.

(2016). This approach partitions the sphere into equal-area cells that are well-suited for our windowing process. A key advantage of this method is that the resulting cells are quasi-rectangular and aligned with parallels and meridians, which greatly simplifies the task of assigning observation points and sources to their respective windows. We leverage this capability to define the set of equal-area windows that serve as the foundation for the iterative, localized inversions. The full procedure is detailed in Algorithm 1.

As highlighted by Soler and Uieda (2021), iterating through the windows in a randomized order is crucial for faster convergence and to avoid spatial artifacts that can arise from a sequential processing order. After iterating through all windows, the accumulated vector $\mathbf{m}$ contains the final estimated magnetic moments for all sources. This window-by-window strategy drastically reduces memory requirements because only the small, local sensitivity matrices ($\tilde{\mathbf{A}}_k$) are ever explicitly constructed, making the method highly scalable for datasets with millions of observations.

2.4 Hyperparameter tuning with block cross-validation for airborne surveys

A crucial step in our methodology is the selection of optimal hyperparameters for the equivalent source model, primarily the depth of the sources and the regularization parameter. In the context of large airborne surveys, this selection is particularly challenging but essential for a robust model (Soler and Uieda, 2021; Uppal et al., 2025). To obtain a realistic assessment of the model's predictive performance, we use block cross-validation, a strategy specifically designed for data with spatial or temporal dependence (Roberts et al., 2017). This method respects the spatial structure of the data by ensuring independence between training and test sets. The survey area is first partitioned into

Algorithm 1 Gradient-Boosted Equivalent Sources on the sphere.

Initialize the global moment vector $\mathbf{p} = \mathbf{0}$.
Define the initial residual vector $\mathbf{r}_0 = \mathbf{d}^o$.
Define an initial set of latitudinal bands, often with constant width (e.g., every 10°).
for each latitudinal band k **do**
    Calculate the central latitude, ϕ_c.
    Determine the number of longitudinal cells, n_k, for the band, such that n_k is proportional to $\cos(\phi_c)$ and is a divisor of 360°.
    Calculate the longitudinal width for cells in this band: $\Delta\lambda_k = 360^\circ / n_k$.
end for
for each window index k in the shuffled list **do**
    Select residuals $\tilde{\mathbf{r}}_{k-1}$ for data points inside the k-th window.
    Compute the local Jacobian matrix $\tilde{\mathbf{A}}_k$ with data points and sources inside the k-th window.
    Solve for the corrective moments $\mathbf{p}_k$:
    $\mathbf{p}_k = (\tilde{\mathbf{A}}_k^\top \tilde{\mathbf{A}}_k + \mu_k \mathbf{I})^{-1} \tilde{\mathbf{A}}_k^\top \tilde{\mathbf{r}}_{k-1}$
    Calculate the global prediction from the local sources: $\mathbf{d}_k = \mathbf{A}_k \mathbf{p}_k$.
    Update the global residuals: $\mathbf{r}_k = \mathbf{r}_{k-1} - \mathbf{d}_k$.
    Accumulate the global solution by adding $\mathbf{p}_k$ to the corresponding entries in $\mathbf{p}$.
end for

non-overlapping spatial blocks. The cross-validation folds are then constructed using these entire blocks, rather than individual points. By training the model on one set of blocks and testing it on a spatially separate set, this approach forces the model to generalize. The resulting error metric of how the model would perform when predicting for a new, unsurveyed area, which is more realistic to use-case scenario.

Our implementation for selecting the optimal set of hyperparameters follows the procedure detailed in Algorithm 2. We define a grid of candidate values for the model hyperparameters. For each combination, a k-fold cross-validation is performed using the spatial blocks to compute an average error score. The set of hyperparameters that minimizes this score is chosen for the final model. This robust validation approach has been successfully applied in recent large-scale equivalent source studies on airborne data to guide the selection of optimal model parameters (Soler and Uieda, 2021; Uppal et al., 2025).

3 Results

3.1 Synthetic data

To evaluate the performance and accuracy of the proposed methodology, we applied it to a synthetic magnetic dataset designed to reproduce realistic survey conditions. The model consists of multiple crustal sources. Specifically, a set of dipoles and dikes with different orientations (W-E, SW-NE, and NW-SE) positioned at varying depths. These sources exhibit both remanent and induced magnetization, generating both regional and local magnetic anomalies. The detailed configuration of the sources is provided in the source code archive (Siqueira-Macedo et al., 2026).

A complex regional magnetic field was generated using a deep distribution of sources. Zero-mean Gaussian noise with a standard deviation corresponding to 5% of the maximum absolute anomaly was added to the data to simulate instrumental and environmental noise. The total field was computed assuming a regional field with inclination -25° and declination -20°, consistent with the mean IGRF values in the study area.

Algorithm 2 Hyperparameter selection using Block K-Fold Cross-Validation

Partition the survey area into a set of L non-overlapping spatial blocks.
Randomly assign the blocks to k folds $\{F_1, F_2, \ldots, F_k\}$.
Define a grid of candidate hyperparameter sets Θ.
Initialize 'min_score' = ∞.
for each hyperparameter set θ in Θ **do**
    Initialize a list of fold scores, 'scores'.
    for $i = 1$ to k **do**
        Set test set to data in blocks from fold F_i; training set to data from all other folds.
        Fit model $\mathbf{p}_i$ on the training set using hyperparameters θ.
        Predict data $\mathbf{d}_{\text{pred}}$ on the coordinates of the test set.
        Calculate score$_i$ (e.g., RMSE) and add it to 'scores'.
    end for
    'avg_score' = mean of 'scores'.
    if 'avg_score' < 'min_score' **then**
        'min_score' = 'avg_score'.
        $\theta^* = \theta$.
    end if
end for
The optimal hyperparameter set is θ^*.

To reproduce a realistic acquisition geometry, the synthetic field was sampled along the flight lines of a public-domain aeromagnetic survey from the Paraná Basin, Brazil. The original dataset, provided by the Agência Nacional do Petróleo (ANP) and distributed through the CPRM/REATE portal (https://reate.cprm.gov.br/anp/TERRESTRE), was preprocessed using a block-reduction procedure. This operation resulted in 507, 395 observation points, whose coordinates were used to generate the synthetic dataset. The resulting total-field anomaly is shown in Figure 3a.

For the modeling process, the equivalent sources in both the deep and shallow layers were defined as magnetic dipoles with an assigned magnetization direction of 90° inclination and 0° declination. The deep layer was estimated from a block-reduced version of the synthetic dataset in order to isolate the long-wavelength components of the magnetic field. A block-reduction procedure based on the mean was applied using a block size of 0.3° in both latitudinal and longitudinal directions, corresponding to approximately 33 km at the equator. This block size represents a compromise between data compression and isolation of regional-scale magnetic trends. As a result, the original dataset containing 507,395 observations was reduced to 795 data points, substantially decreasing the computational cost of the deep-layer inversion while preserving the long-wavelength magnetic signal (Figure 3b).

The hyperparameters of the deep layer were selected through a block K-fold cross-validation procedure applied to the block-reduced dataset. The tested parameter space comprised five relative depths ranging from approximately 90 km to 270 km and five damping values varying from 10^2 to 10^6, resulting in 25 parameter combinations. Spatial blocks of 1° (approximately 111 km) were used to avoid the spatial dependence between samples in the training and testing sets during the cross-validation process. The cross-validation results are shown in Figure 4a. The minimum RMSE of 83.6 was obtained for a relative depth of approximately 135 km and a damping value of 10^3. The error surface exhibits a well-defined minimum around this configuration, indicating limited sensitivity to moderate variations in the hyperparameters and suggesting a stable regional-field solution.

Using the selected hyperparameters, the deep-layer inversion was performed using the entire block-reduced dataset. The resulting model represents the regional magnetic field and is shown in

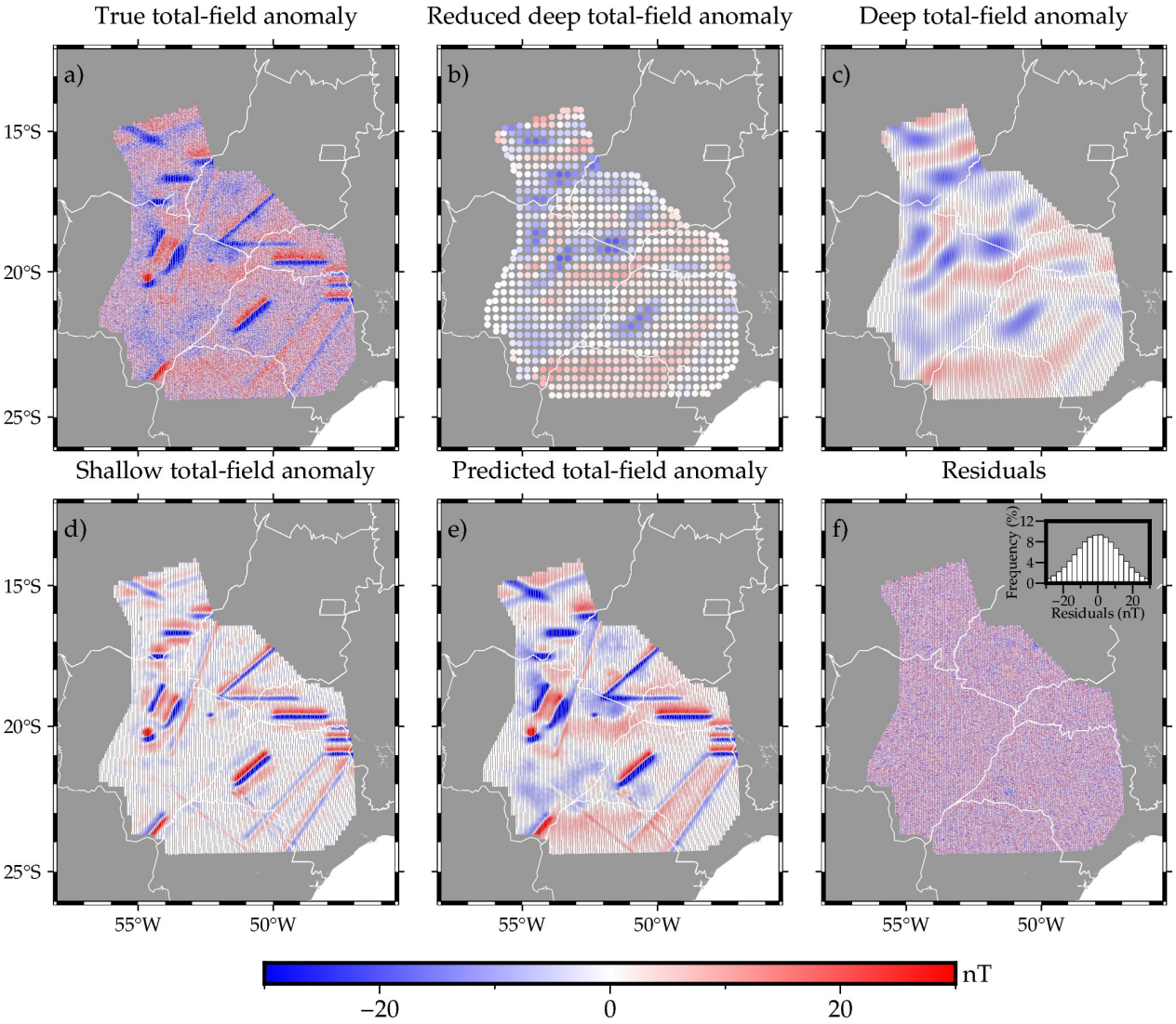


Figure 3: Illustration of the dual-layer decomposition process. **a)** True total-field anomaly. **b)** Deep total-field anomaly, capturing the long-wavelength regional field. **c)** Deep total-field anomaly, predicted on all data points. **d)** Shallow total-field anomaly, capturing the short-wavelength local anomalies. **e)** Predicted total-field anomaly. **f)** Residuals of the predicted model.

Figure 3b. The deep-layer was then used to predict the total-field anomaly onto the full observation coordinates. The residuals between the original data and the deep-layer prediction were computed, these residuals constitute the input for the shallow-layer inversion.

The shallow layer was estimated using an iterative gradient-boosting algorithm applied to the residuals of the deep layer. A window size of 2° (approximately 220 km) was adopted to limit the memory usage of the inversion to the amount of RAM available.

Performing cross-validation on the entire residual dataset would be computationally heavy due to the large number of observations. However, since the deep layer removes most of the long-wavelength signal, the remaining residuals are dominated by local magnetic effects. Therefore, a representative subset of the data was selected for hyperparameter tuning. This subset was obtained by cropping the residual dataset to the region bounded by longitudes −54° to −52° and latitudes −17° to −16°, resulting in 15,307 observation points. This area contains a representative range of anomaly amplitudes and wavelengths, preserving the spatial variability required for robust cross-

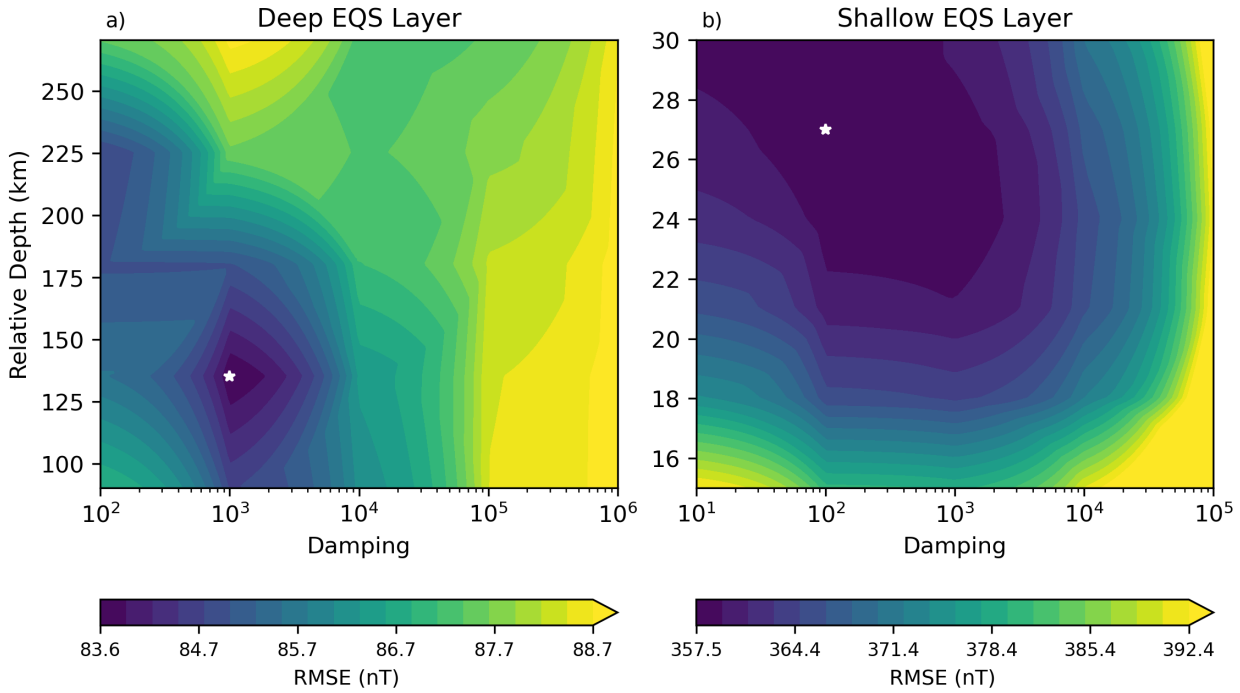


Figure 4: Block K-fold cross-validation results for the synthetic dataset. **a)** RMSE as a function of damping and relative depth for the deep equivalent sources layer, computed using the block-reduced dataset. **b)** RMSE obtained for the shallow layer using a cropped subset of the residual data. White stars indicate the selected optimal hyperparameter combinations corresponding to the minimum RMSE in each panel.

validation. A block K-fold cross-validation was then applied to this subset using spatial blocks of 0.1° (approximately 12 km). This configuration ensures that neighboring observations are not simultaneously used for training and validation, reducing spatial bias. The tested hyperparameters comprised six relative depths ranging from 15 km to 30 km and five damping values varying from 10^1 to 10^5, resulting in 30 parameter combinations. The cross-validation results are shown in Figure 4b. The minimum RMSE of 357.5 was obtained for a relative depth of approximately 27 km and a damping value of 10^2. In contrast to the deep layer, the RMSE surface exhibits a less well-defined minimum, highlighting the decreased sensitivity of near-surface sources to parameter variations.

The selected parameters were then applied to invert the full residual dataset, producing the predicted total-field anomaly of the shallow-layer model shown in Figure 3d. The final residuals, obtained after combining the deep and shallow predictions and subtracting them from the true data, are presented in Figure 3e. The low amplitude and spatially incoherent distribution of the residuals indicate that the main magnetic features were successfully modeled.

The estimated deep and shallow layers were then used to predict the magnetic field onto a regular grid with a spatial resolution of 0.009° (approximately 1 km), constant height of 500 m, and dimensions of 1223 × 1057, totaling 3,878,133 points. In addition to the total-field anomaly, the eastward (B_E), northward (B_N), and upward (B_U) components were also predicted. The predicted grids are shown in Figure 5a–d, together with the true synthetic fields in Figure 5e–h and the difference between the true and predicted in Figure 5i–l. The difference maps exhibit low amplitudes and are largely free of coherent spatial patterns within the main data coverage area, indicating an accurate reconstruction of the observed magnetic field. Outside the core survey region, moderately increased residuals reflect edge effects and reduced data support near the survey boundaries. In

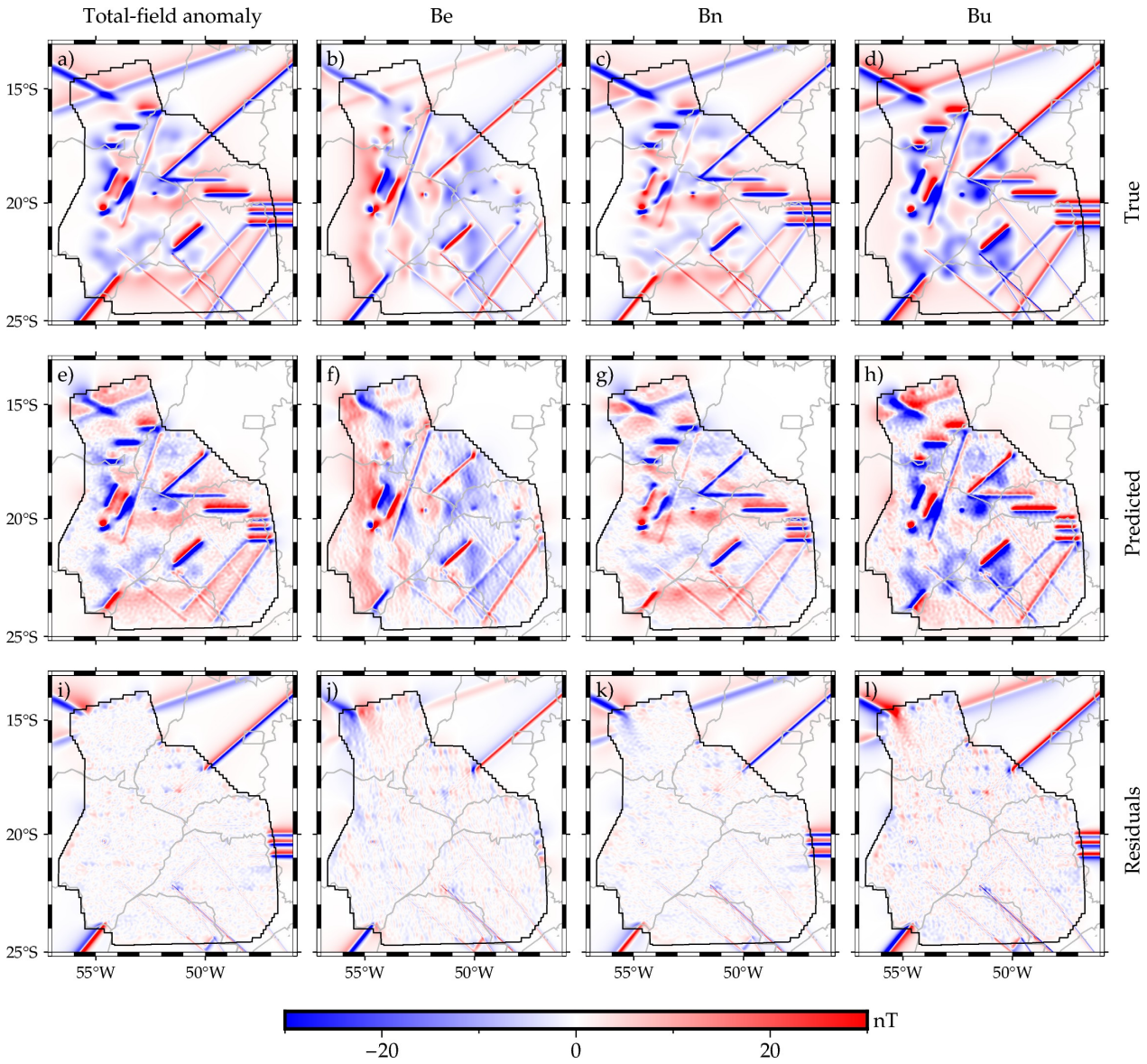


Figure 5: Gridded interpolation results for the total-field anomaly and its vector components (Be, Bn, Bu). The first row **(a-d)** shows the true synthetic fields ("True"). The second row **(e-h)** shows the fields predicted ("Predicted") by the dual-layer model. The third row **(i-l)** shows the final residuals ("Residuals"), corresponding to the difference between the true and predicted fields.

regions dominated by high-frequency anomalies associated with very shallow dike systems, localized residuals are still observed, indicating that, despite the use of a dual-layer parameterization, the extremely shallow nature of these sources poses challenges for complete recovery. Nevertheless, the proposed approach provides a robust alternative to derivative-based transformations commonly used in magnetic data processing and inversion, which are known to strongly amplify measurement noise and acquisition-related artifacts. By estimating the full vector components directly from total-field anomaly data through physically constrained equivalent-source modeling, the method enables the use of physically meaningful field attributes as inputs for subsequent inversion and interpretation procedures. This strategy allows the enhancement of short-wavelength features while preserving numerical stability, avoiding the instability typically introduced by high-order spatial derivatives. As a result, the predicted field components constitute a reliable basis for further quantitative anal-

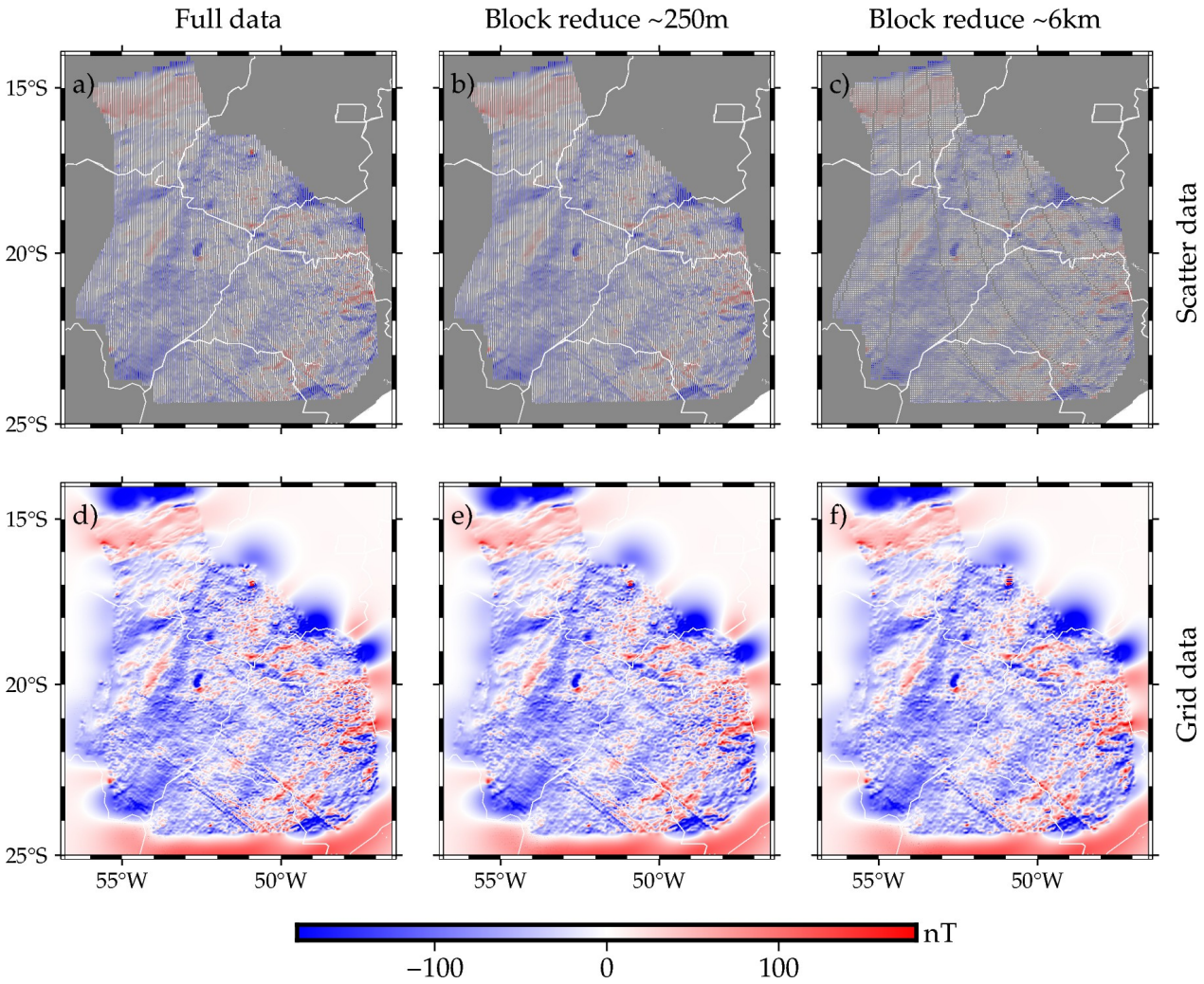


Figure 6: Effect of varying block-mean size on the predicted total-field anomaly for the same region used in the Paraná Basin ANP data. **a–c)** Observed total-field anomaly gridded from different block-mean decimations. **e–f)** Predicted total-field anomaly using the spherical dual-layer gradient-boosted equivalent sources.

ysis, particularly in high-noise environments where traditional derivative operators often become unreliable.

The complete workflow, including the dual-layer inversion of 507,395 observations and prediction over 3,878,133 grid points, was completed in under 120 minutes on a personal computer equipped with an Intel® Core™ i5-9300H CPU @ 2.40 GHz (8 cores) and 16 GB of RAM, demonstrating the suitability of the proposed methodology for processing large-scale magnetic datasets.

3.2 Real Data Application

To evaluate the performance of the proposed methodology under realistic conditions, it was applied to airborne magnetic data acquired over the Paraná Basin, Brazil. The dataset, provided by the Agência Nacional do Petróleo (ANP; https://reate.cprm.gov.br/anp/TERRESTRE), covers latitudes from −24.14° to −14.14° and longitudes from −56.44° to −46.96°, encompassing one of the largest sedimentary basins in South America. Data acquisition was conducted along north–south flight lines spaced approximately 6 km apart, with east–west control lines every 18 km, at an average altitude of 1800 m. Horizontal and vertical positioning were obtained using GPS, ensuring high positional

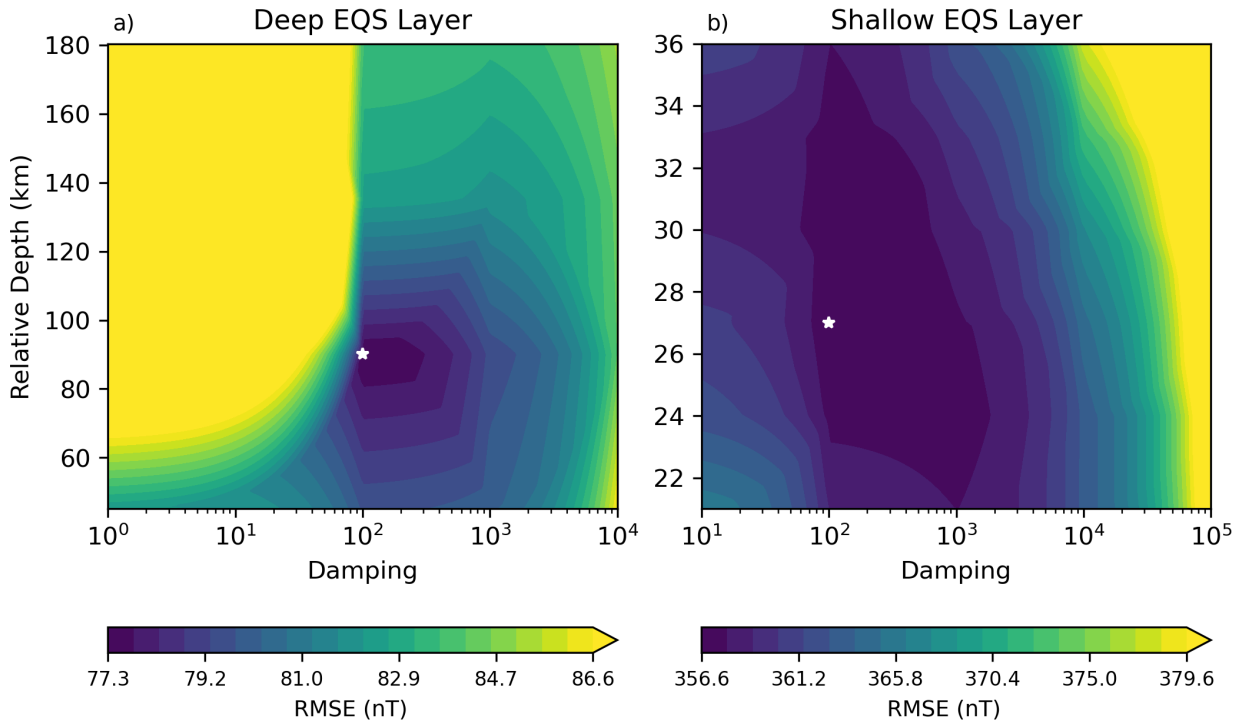


Figure 7: Block K-fold cross-validation results for the real dataset. **a)** RMSE as a function of damping and relative depth for the deep equivalent sources layer, computed using the block-reduced dataset. **b)** RMSE obtained for the shallow layer using a cropped subset of the residual data. White stars indicate the selected optimal hyperparameter combinations corresponding to the minimum RMSE in each panel.

accuracy. According to the official processing report, the data were fully levelled using Oasis Montaj following a two-stage procedure to minimize differences at flight line intersections. The dataset was originally referenced to the SAD-69 datum and subsequently converted to WGS-84 by the data provider. The original raw data were sampled at 100 Hz, which results in approximately one data points every 8 cm. This leads to an unnecessarily large dataset given the 6 km line spacing. Hence, we decimated the data to 1 Hz by averaging consecutive groups of 100 samples along each flight line. Numerical variables in the dataset were averaged, while categorical and identifier fields were retained from the central record of each block. Records containing corrupted or inconsistent values were discarded. This procedure preserves along-line continuity while significantly reducing the dataset size. In addition, tie lines were removed because they exhibited inconsistent amplitude values, being entirely positive and showing amplitudes ten times greater than the flight line data, introducing spurious variations and systematic distortions in the magnetic signal that could negatively affect the equivalent sources modeling. After this preprocessing step, the resulting dataset with 1,636,695 observations is illustrated in Figure 6a.

Our target is to produce a regular grid at a constant height of 500 m and a grid spacing of 0.0023° (approximately 250 m). The sampling density along flight lines of the 1 Hz data is larger than the desired grid resolution. Therefore, we investigated the sensitivity of the interpolation results to different levels of data decimation. The data were decimated using a block-mean operation with two different block sizes, leading to three different configurations: the complete dataset without decimation (Figure 6a), block size of 0.0023° (approximately 250 m; Figure 6b), and block size of 0.06° (approximately 6.6 km; Figure 6c). All datasets were used to generate final grids with 0.0023° resolution. We used the same processing workflow for all datasets, which was the same as the one applied

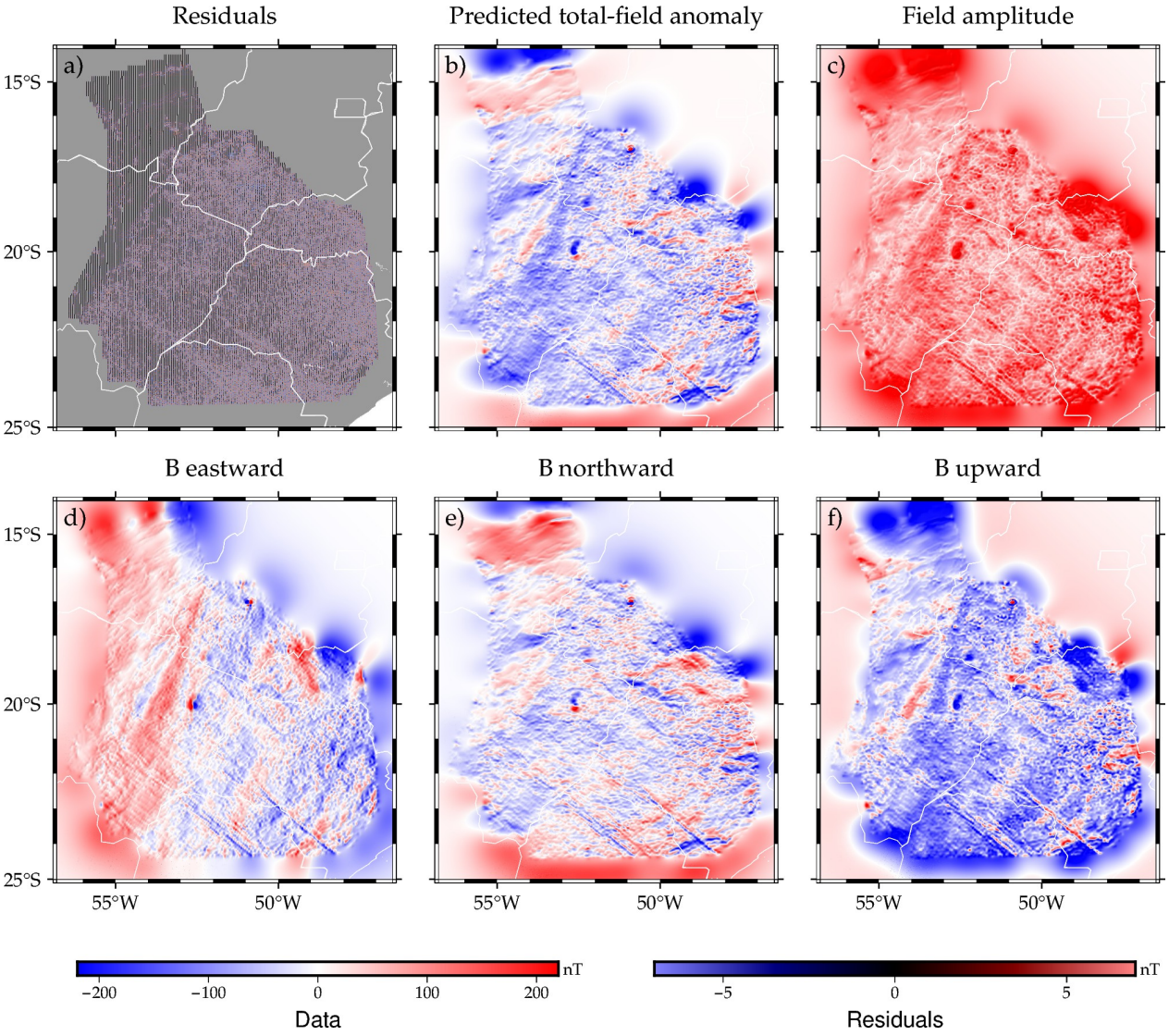


Figure 8: Predicted magnetic field for the Paraná Basin dataset. (**a**) Total-field anomaly. (**b**) Amplitude of the anomalous magnetic field. (**d**–**f**) East, north, and upward components of the magnetic field. The smooth spatial behavior and coherence between components indicate the numerical stability of the proposed modeling approach.

to the synthetic data. The deep layer was estimated from a block-mean version of each dataset using a block size of 0.1°, corresponding to approximately 11 km, in order to isolate the long-wavelength signal. For the cross-validation, we used spatial blocks of 0.45° (approximately 50 km) for the deep layer and blocks of 0.18° (approximately 20 km) for the shallow layer. In addition, a window size of 1.5° was used in the gradient-boosting procedure of the shallow layer to control the amount of data processed in each iteration, ensuring efficient memory usage and computational stability. The details of the cross-validation procedure for each dataset can be found in the source code archive (Siqueira-Macedo et al., 2026). Using the same workflow for all three data decimation levels allows a direct comparison of the outputs since source depth and damping regularization are dependent on the input data geometry.

The predicted grids obtained from the different decimation levels are shown in Figure 6d–f. The coarsest block-mean decimation (0.06°) shown in Figure 6f resulted in the shortest processing time (approximately 52 minutes). However, it significantly attenuated short-wavelength magnetic anoma-

lies, compromising the recovery of near-surface sources and limiting its practical applicability. In contrast, the finest block-mean decimation (0.0023°) shown in Figure 6e, corresponding to the target grid resolution, required a processing time of approximately 10 hours and 48 minutes and produced results that are nearly indistinguishable from those obtained using the full dataset (Figure 6d), which required approximately 13 hours and 49 minutes. Despite the higher computational cost, the 0.0023° block-mean decimation provides a roughly 20% reduction in processing time relative to the full dataset, while preserving the dominant short- and long-wavelength magnetic features.

While the grids produced from the complete dataset and the data decimated at 0.0023° appear visually identical at a regional scale, closer inspection of the short-wavelength features reveals the true impact of the decimation strategy. The coarser block-mean decimation (0.06°) significantly smooths out the sharp, high-frequency anomalies associated with near-surface sources. In contrast, decimation using a block size compatible with the final grid resolution (0.0023°) exceptionally preserves these high-frequency details, yielding results strictly equivalent to the full dataset but with enhanced computational efficiency. Based on this optimal trade-off between minimizing processing time and maximizing spectral preservation, the dataset decimated at 0.0023° was selected for the subsequent analyses. The hyperparameters of the deep layer were selected through a block K-fold cross-validation procedure. The tested parameter space comprised damping values of 1, 100, and 10,000 and source depths of 70 km, 100 km, and 130 km, resulting in nine parameter combinations. The cross-validation results are shown in Figure 7a. The minimum RMSE of 77.3 was obtained for a relative depth of 100 km and a damping value of 100. The error surface exhibits a well-defined minimum, indicating high sensitivity to moderate hyperparameter variations. The shallow layer was estimated using an iterative gradient-boosting algorithm applied to the deep-layer residuals. Due to the large number of observations, cross-validation on the entire residual dataset would be computationally prohibitive. Therefore, a representative subset was selected for hyperparameter tuning by cropping the residual data to the region bounded by longitudes −54° to −50° and latitudes −18° to −16°. A block K-fold cross-validation was applied to this subset. The tested hyperparameters comprised damping values of 10^2, 10^4, and 10^6 and source depths of 6 km, 9 km, and 12 km, resulting in nine parameter combinations. The cross-validation results are shown in Figure 7b. The minimum RMSE of 356.6 was obtained for the optimal shallow-layer configuration of damping equal to 10^4 and relative source depth of 9 km. The selected parameters were then applied to invert the full residual dataset, producing the shallow-layer model. The final residuals (Figure 8a), obtained after combining the deep and shallow predictions, exhibit low amplitudes and lack coherent spatial structures.

The estimated deep and shallow layers were subsequently used to predict the magnetic field onto a regular grid with a spatial resolution of 0.0023° (approximately 250 m) and a constant height of 500 m. In addition to the total-field anomaly (Figure 8b), the amplitude (norm) of the magnetic field (Figure 8c) and the eastward (B_E), northward (B_N), and upward (B_U) components (Figure 8d–f) were also computed. The magnetic field amplitude centralizes the dipolar anomalies, highlighting anomaly sources in a similar fashion to the total gradient amplitude. The B_E component emphasizes predominantly north–south-oriented features, whereas the B_N component enhances east–west-trending structures. The B_U component also exhibits mostly centered anomalies, consistent with the distribution observed in the total-field anomaly and amplitude maps. Together, these results confirm the ability of the proposed methodology to recover multiple components of the anomalous magnetic field from observations of the total-field anomaly.

A comprehensive summary of the hyperparameters and processing variables used throughout our methodology, for both synthetic and real data applications, is presented in Table 1.

Table 1: Summary of the hyperparameters and processing parameters used for the dual-layer equivalent sources inversion in both synthetic and real data applications.

Layer	Parameter	Synthetic Data	Real Data
Deep	Data decimation block size	0.3° (~33 km)	0.1° (~11 km)
	Window size	N/A (entire dataset)	N/A (entire dataset)
	CV spatial block size	1° (~111 km)	0.45° (~50 km)
	Tested depth range	90–270 km	70–130 km
	Optimal relative depth	135 km	100 km
	Tested damping range	10^2–10^6	10^0–10^4
	Optimal damping	10^3	10^2
Shallow	Gradient-boosting window	2° (~220 km)	1.5° (~166 km)
	CV spatial block size	0.1° (~12 km)	0.18° (~20 km)
	Tested depth range	15–30 km	6–12 km
	Optimal relative depth	27 km	9 km
	Tested damping range	10^1–10^5	10^2–10^6
	Optimal damping	10^2	10^4

4 Discussion

The synthetic data experiments demonstrated that the dual-layer configuration provides a robust mechanism for separating long- and short-wavelength magnetic components under realistic acquisition geometries and noise conditions. The adopted data decimation strategy for the deep layer reduced the original dataset from more than 500,000 observations to fewer than 1,000 points while preserving the dominant regional signal. This reduction enabled efficient hyperparameter tuning and inversion without compromising spectral fidelity. Cross-validation results obtained from the synthetic dataset showed a well-defined minimum for the deep layer, indicating a stable solution. The cross-validation of the shallow layer exhibited a less well-defined minimum, reflecting the decreased sensitivity of near-surface sources to depth and regularization. These results highlight the importance of independent parameter tuning and justify the adoption of separate optimization strategies for regional and local components. Moreover, our synthetic data results show that our spherical dual-layer method is able to accurately recover the magnetic field components from the total-field anomaly observations. This was shown to be theoretically possible through the use of Fourier transform by Lima and Weiss (2009) and through the use of equivalent sources by Li et al. (2020). Here, we demonstrate that this can also be achieved in a spherical or geodetic reference frame through the use of equivalent sources.

The application to real airborne magnetic data from the Paraná Basin confirmed the scalability and robustness of the proposed workflow under realistic conditions, including heterogeneous sampling density, acquisition artifacts, and large data volumes (upward of 1.5 million data points). A detailed analysis of different spatial decimation strategies demonstrated that decimation using coarse block sizes (of the order of the line spacing), although computationally efficient, leads to significant attenuation of short-wavelength anomalies and compromises the recovery of near-surface

sources. Conversely, data decimation using a block size that is compatible with the final grid resolution preserved the amplitude of short-wavelength anomalies and resulted in a grid that is largely indistinguishable from the one produced with the full dataset. Moreover, the processing time for the reduced dataset was approximately 20% smaller than for the full dataset. Therefore, we recommend always decimating the input data using a block mean operation with block size equal to the desired grid spacing (Smith and Wessel, 1990).

The availability of vector components provides some advantages over traditional derivative-based interpretation techniques. Magnetic derivatives are inherently sensitive to noise, interpolation artifacts, and uneven data coverage, particularly in continental-scale surveys. In contrast, the equivalent-source-based predicted field components and amplitude produces smooth, physically constrained fields that retain geological meaning while avoiding noise amplification. The anomalous field amplitude is particularly useful for interpretation and geometry inversion workflows. As demonstrated by Hidalgo-Gato et al. (2021), the inversion of basement relief from the amplitude of the magnetic field is only weakly dependent on the often unknown magnetization direction. This characteristic allows reliable structural characterization even in the presence of remanent magnetization and limited prior information. Consequently, the framework proposed here offers a solid foundation for subsequent structural mapping, susceptibility inversion, and integrated geophysical modeling.

5 Conclusions

This study presented and systematically validated a spherical equivalent sources framework for large-scale magnetic data continuation, interpolation, and transformation. The proposed methodology integrates dual-layer equivalent sources modeling (Uppal et al., 2025), gradient-boosting (Soler and Uieda, 2021), and spatial cross-validation into a unified and computationally efficient workflow. Our equivalent sources formulation can work with data in both spherical and geodetic coordinate systems.

Overall, the results indicate that the spherical dual-layer gradient-boosted equivalent sources method constitutes a flexible, scalable, and physically consistent solution for magnetic data processing. The framework is capable of handling very large datasets while preserving short- and long-wavelength of the magnetic field and maintaining manageable computational requirements. The method proposed here is able to handle millions of data points in a modest computer in the timescale of hours. However, the spherical calculations are significantly slower than their Cartesian counterparts. Thus, the current formulation will likely struggle to process larger compilations involving multiple surveys and tens to hundreds of millions of data points without access to significant computational resources. Further optimization of the equivalent sources methods would be required to make it feasible to use our method to generate a consistent and integrated model for continental scale data compilations. Additionally, future work will focus on a comprehensive quantitative comparison between our spherical framework and traditional Cartesian approaches. This comparison will allow us to rigorously assess the impact of map projection distortions and Earth's curvature on large-scale magnetic modeling.

Open research

The Python source code used to produce all results and figures presented in this study is available at https://github.com/compgeolab/eqs-magnetic-spherical and https://doi.org/10.5281/zenodo.1850984

4 under the MIT open-source license.

This research made use of the following open-source scientific software: NumPy (Harris et al., 2020) for numerical computing and linear algebra, Matplotlib (Hunter, 2007) and PyGMT (Tian et al., 2026) for visualization and map generation, Pandas (The pandas development team, 2024) for tabular data handling, Xarray (Hoyer and Hamman, 2017) for working with gridded datasets, Pooch (Uieda et al., 2020) for downloading and caching data, Verde (Uieda, 2018) for spatial interpolation and data decimation, Bordado (Fatiando a Terra Project and Uieda, 2025) for moving window operations, Harmonica (Fatiando a Terra Project et al., 2024b) for potential field data processing and modelling, Boule (Fatiando a Terra Project et al., 2024a) for ellipsoids and coordinate conversions, and Jupyter Notebooks (Granger and Pérez, 2021; Thomas et al., 2016) for code development and documentation.

The aeromagnetic data used in this study are publicly available from the Brazilian National Agency of Petroleum, Natural Gas and Biofuels (ANP) and the Geological Survey of Brazil (CPRM) through the REATE platform at https://reate.cprm.gov.br/anp/TERRESTRE.

Acknowledgements

We are indebted to the developers and maintainers of the open-source software without which this work would not have been possible. ASM was supported by scholarship 88887.947899/2024-00 from Coordenação de Aperfeiçoamento de Pessoal de Nível Superior (CAPES). LU was supported in part by start-up grant PRPI 22.1.09345.01.2 from Universidade de São Paulo. We are grateful to Santiago R. Soler, Gelson F. Souza-Junior, Yago M. Castro, Vanderlei C. Oliveira Jr., and Marco Couto Junior for discussions that helped shape and refine this research. We also thank editor Mark Dekkers, reviewer Maximilian Lowe and an annonymous reviewer for their feedback on the original manuscript.

Conflict of interest

The authors declare no conflict of interest. ASM was supported by scholarship 88887.947899/2024-00 from Coordenação de Aperfeiçoamento de Pessoal de Nível Superior (CAPES). LU was supported in part by start-up grant PRPI 22.1.09345.01.2 from Universidade de São Paulo.

References

Alldredge, L. R. and Stearns, C. O. (1969). Dipole model of the sources of the earth's magnetic field and secular change. *Journal of Geophysical Research*, 74(27):6583–6593. doi:10.1029/jb074i027p06583. URL http://dx.doi.org/10.1029/JB074i027p06583.

Barnes, G. and Lumley, J. (2011). Processing gravity gradient data. *GEOPHYSICS*, 76(2):I33–I47. doi:10.1190/1.3548548.

Blakely, R. J. (1995). *Potential Theory in Gravity and Magnetic Applications*. Cambridge University Press. ISBN 9780511549816. doi:10.1017/cbo9780511549816.

Cordell, L. (1992). A scattered equivalent-source method for interpolation and gridding of potential-field data in three dimensions. *GEOPHYSICS*, 57(4):629–636. doi:10.1190/1.1443275.

Dampney, C. N. G. (1969). THE EQUIVALENT SOURCE TECHNIQUE. *GEOPHYSICS*, 34(1):39–53. doi:10.1190/1.1439996.

Dyment, J. and Arkani-Hamed, J. (1998). Equivalent source magnetic dipoles revisited. *Geophysical*

Research Letters, 25(11):2003–2006. doi:10.1029/98gl51331. URL http://dx.doi.org/10.1029/98GL51331.

Ebbing, J., Dilixiati, Y., Haas, P., Ferraccioli, F., and Scheiber-Enslin, S. (2021). East antarctica magnetically linked to its ancient neighbours in gondwana. *Scientific Reports*, 11(1). doi:10.1038/s41598-021-84834-1.

Emilia, D. A. (1973). Equivalent sources used as an analytic base for processing total magnetic field profiles. *GEOPHYSICS*, 38(2):339–348. doi:10.1190/1.1440344.

Fatiando a Terra Project, Bucha, B., Dinneen, C., Gomez, M., Li, L., Pesce, A., Soler, S. R., Uieda, L., and Wieczorek, M. (2024a). Boule: Reference ellipsoids for geodesy and geophysics (version 0.5.0) [Software]. doi:10.5281/ZENODO.3530749.

Fatiando a Terra Project, Castro, Y. M., Esteban, F. D., Li, L., Oliveira Jr, V. C., Pesce, A., Shea, N., Soler, S. R., Souza-Junior, G. F., Tankersley, M., Uieda, L., and Uppal, I. (2024b). Harmonica: Forward modeling, inversion, and processing gravity and magnetic data (version 0.7.0)[software]. doi:10.5281/ZENODO.13308312.

Fatiando a Terra Project and Uieda, L. (2025). Bordado: Create, manipulate, and split coordinates (Version 0.4.0) [Software]. doi:10.5281/ZENODO.15051755.

Gorski, K. M., Hivon, E., and Wandelt, B. D. (1998). Analysis issues for large cmb data sets. doi:10.48550/ARXIV.ASTRO-PH/9812350.

Granger, B. E. and Pérez, F. (2021). Jupyter: Thinking and storytelling with code and data. *Computing in Science & Engineering*, 23(2):7–14. doi:10.1109/mcse.2021.3059263.

Guspí, F. and Novara, I. (2009). Reduction to the pole and transformations of scattered magnetic data using newtonian equivalent sources. *GEOPHYSICS*, 74(5):L67–L73. doi:10.1190/1.3170690.

Harris, C. R., Millman, K. J., van der Walt, S. J., Gommers, R., Virtanen, P., Cournapeau, D., Wieser, E., Taylor, J., Berg, S., Smith, N. J., Kern, R., Picus, M., Hoyer, S., van Kerkwijk, M. H., Brett, M., Haldane, A., del Río, J. F., Wiebe, M., Peterson, P., Gérard-Marchant, P., Sheppard, K., Reddy, T., Weckesser, W., Abbasi, H., Gohlke, C., and Oliphant, T. E. (2020). Array programming with numpy. *Nature*, 585(7825):357–362. doi:10.1038/s41586-020-2649-2.

Heincke, B. H., Szwillus, W., Freienstein, J., Ebbing, J., Gaina, C., Ruppel, A., Dilixiati, Y., and Wansing, A. (2026). A new magnetic anomaly map for greenland based on a combination of equivalent source modeling and spherical harmonic expansion. *Earth System Science Data*, 18(3):1943–1967. doi:10.5194/essd-18-1943-2026. URL http://dx.doi.org/10.5194/essd-18-1943-2026.

Hidalgo-Gato, M. C., Barbosa, V. C. F., and Oliveira, V. C. (2021). Magnetic amplitude inversion for depth-to-basement and apparent magnetization-intensity estimates. *GEOPHYSICS*, 86(1):J1–J11. doi:10.1190/geo2019-0726.1.

Hoyer, S. and Hamman, J. (2017). xarray: N-d labeled arrays and datasets in python. *Journal of Open Research Software*, 5(1):10. doi:10.5334/jors.148.

Hunter, J. D. (2007). Matplotlib: A 2d graphics environment. *Computing in Science & Engineering*, 9(3):90–95. doi:10.1109/mcse.2007.55.

Jirigalatu, J. and Ebbing (2019). A fast equivalent source method for airborne gravity gradient data. *GEOPHYSICS*, 84(5):G75–G82. doi:10.1190/geo2018-0366.1.

Kother, L., Hammer, M. D., Finlay, C. C., and Olsen, N. (2015). An equivalent source method for modelling the global lithospheric magnetic field. *Geophysical Journal International*, 203(1):553–566. doi:10.1093/gji/ggv317.

Langel, R. A. and Hinze, W. J. (1998). *The magnetic field of the Earth's lithosphere: The satellite perspective*. Cambridge University Press. doi:10.1017/cbo9780511629549.006.

Leão, J. W. D. and Silva, J. B. C. (1989). Discrete linear transformations of potential field data. *GEOPHYSICS*, 54(4):497–507. doi:10.1190/1.1442676.

Li, D., Liang, Q., Du, J., Sun, S., Zhang, Y., and Chen, C. (2020). Transforming total-field magnetic anomalies into three components using dual-layer equivalent sources. *Geophysical Research Letters*, 47(3). doi:10.1029/2019gl084607.

Li, D., Liu, X., Zhai, Z., Du, J., Chen, C., Ma, J., and Wang, Y. (2023). A stable downward continuation method for processing gravity data using the equivalent sources with compactness and smoothing constraints. *Journal of Applied Geophysics*, 215:105128. doi:10.1016/j.jappgeo.2023.105128.

Li, J. and Morozov, I. (2006). Continuous equivalent source method of 3d potential field data. In *SEG Technical Program Expanded Abstracts 2006*, page 914–918. Society of Exploration Geophysicists. doi:10.1190/1.2370405.

Li, Y. (2001). Processing gravity gradiometer data using an equivalent source technique. In *SEG Technical Program Expanded Abstracts 2001*, volume 34, page 1466–1469. Society of Exploration Geophysicists. doi:10.1190/1.1816382.

Li, Y. and Oldenburg, D. W. (2010). Rapid construction of equivalent sources using wavelets. *GEOPHYSICS*, 75(3):L51–L59. doi:10.1190/1.3378764.

Lima, E. A. and Weiss, B. P. (2009). Obtaining vector magnetic field maps from single-component measurements of geological samples. *Journal of Geophysical Research: Solid Earth*, 114(B6). doi:10.1029/2008jb006006.

Malkin, Z. (2016). A new method to subdivide a spherical surface into equal-area cells. doi:10.48550/ARXIV.1612.03467.

Mayhew, M., Johnson, B., and Langel, R. (1980). An equivalent source model of the satellite-altitude magnetic anomaly field over australia. *Earth and Planetary Science Letters*, 51(1):189–198. doi:10.1016/0012-821x(80)90266-6. URL http://dx.doi.org/10.1016/0012-821X(80)90266-6.

Mayhew, M. A. (1979). Inversion of satellite magnetic anomaly data. *Journal of Geophysics*, 45(2):119–128.

Mayhew, M. A. (1982). Application of satellite magnetic anomaly data to curie isotherm mapping. *Journal of Geophysical Research: Solid Earth*, 87(B6):4846–4854. doi:10.1029/jb087ib06p04846. URL http://dx.doi.org/10.1029/JB087iB06p04846.

Mendonça, C. A. (2020). Subspace method for solving large-scale equivalent layer and density mapping problems. *GEOPHYSICS*, 85(3):G57–G68. doi:10.1190/geo2019-0302.1.

Mendonça, C. A. and Silva, J. B. C. (1994). The equivalent data concept applied to the interpolation of potential field data. *GEOPHYSICS*, 59(5):722–732. doi:10.1190/1.1443630.

Mendonça, C. A. and Silva, J. B. C. (1995). Interpolation of potential-field data by equivalent layer and minimum curvature: A comparative analysis. *GEOPHYSICS*, 60(2):399–407. doi:10.1190/1.1443776.

Oliveira Jr., V. C., Barbosa, V. C. F., and Uieda, L. (2013). Polynomial equivalent layer. *GEOPHYSICS*, 78(1):G1–G13. doi:10.1190/geo2012-0196.1.

Oliveira Junior, V. C., Takahashi, D., Reis, A. L. A., and Barbosa, V. C. F. (2023). Computational aspects of the equivalent-layer technique: review. *Frontiers in Earth Science*, 11. doi:10.3389/feart.2023.1253148.

O'Brien, M. S. and Parker, R. L. (1994). Regularized geomagnetic field modelling using monopoles. *Geophysical Journal International*, 118(3):566–578. doi:10.1111/j.1365-246x.1994.tb03985.x.

Reilly, J. P. and Herbrechtsmeier, E. H. (1978). A systematic approach to modeling the geopotential with point mass anomalies. *Journal of Geophysical Research: Solid Earth*, 83(B2):841–844. doi:10.1029/jb083ib02p00841. URL http://dx.doi.org/10.1029/JB083iB02p00841.

Roberts, D. R., Bahn, V., Ciuti, S., Boyce, M. S., Elith, J., Guillera-Arroita, G., Hauenstein, S., Lahoz-Monfort, J. J., Schröder, B., Thuiller, W., Warton, D. I., Wintle, B. A., Hartig, F., and Dormann, C. F. (2017). Cross-validation strategies for data with temporal, spatial, hierarchical, or phylogenetic structure. *Ecography*, 40(8):913–929. doi:10.1111/ecog.02881.

Silva, J. B. C. (1986). Reduction to the pole as an inverse problem and its application to low-latitude anomalies. *GEOPHYSICS*, 51(2):369–382. doi:10.1190/1.1442096.

Siqueira, F. C. L., Oliveira Jr., V. C., and Barbosa, V. C. F. (2017). Fast iterative equivalent-layer technique for gravity data processing: A method grounded on excess mass constraint. *GEOPHYSICS*, 82(4):G57–G69. doi:10.1190/geo2016-0332.1.

Siqueira-Macedo, A., Uieda, L., and Uppal, I. (2026). Supplementary material for "Magnetic dual-layer equivalent sources on the sphere" [Dataset]. doi:10.5281/zenodo.18509844.

Smith, W. H. F. and Wessel, P. (1990). Gridding with continuous curvature splines in tension. *Geophysics*, 55(3):293–305. doi:10.1190/1.1442837.

Soler, S. R. and Uieda, L. (2021). Gradient-boosted equivalent sources. *Geophysical Journal International*, 227(3):1768–1783. doi:10.1093/gji/ggab297.

Takahashi, D., Oliveira Jr., V. C., and Barbosa, V. C. F. (2020). Convolutional equivalent layer for gravity data processing. *GEOPHYSICS*, 85(6):G129–G141. doi:10.1190/geo2019-0826.1.

Takahashi, D., Oliveira Jr., V. C., and Barbosa, V. C. F. (2022). Convolutional equivalent layer for magnetic data processing. *GEOPHYSICS*, 87(5):E291–E306. doi:10.1190/geo2021-0599.1.

The pandas development team (2024). pandas-dev/pandas: Pandas (version 3.0.3)[software]. *Zenodo*. doi:10.5281/ZENODO.13819579.

Thomas, K., Benjamin, R.-K., Fernando, P., Brian, G., Matthias, B., Jonathan, F., Kyle, K., Jessica, H., Jason, G., Sylvain, C., Paul, I., Damián, A., Safia, A., Carol, W., and Team, J. D. (2016). *Jupyter Notebooks – publishing format for reproducible computational workflows*. IOS Press. doi:10.3233/978-1-61499-649-1-87.

Tian, D., Fröhlich, Y., Leong, W. J., Grund, M., Schlitzer, W., Jones, M., Uieda, L., and Luis, J. M. F. (2026). PyGMT: Bridging Python and the Generic Mapping Tools for Geospatial Visualization and Analysis. *Geochemistry, Geophysics, Geosystems*, 27(7). doi:10.1029/2026gc013105.

Uieda, L. (2018). Verde: Processing and gridding spatial data using green's functions. *Journal of Open Source Software*, 3(30):957. doi:10.21105/joss.00957.

Uieda, L., Soler, S., Rampin, R., van Kemenade, H., Turk, M., Shapero, D., Banihirwe, A., and Leeman, J. (2020). Pooch: A friend to fetch your data files. *Journal of Open Source Software*, 5(45):1943. doi:10.21105/joss.01943.

Uppal, I., Uieda, L., Oliveira Jr., V., and Holme, R. (2025). Transforming total field anomaly into anomalous magnetic field: Using dual-layer gradient-boosted equivalent sources. *EarthArXiv*. doi:10.31223/x58b1q.

Vermeille, H. (2002). Direct transformation from geocentric coordinates to geodetic coordinates. *Journal of Geodesy*, 76(8):451–454. doi:10.1007/s00190-002-0273-6.

von Frese, R. R., Hinze, W. J., and Braile, L. W. (1981). Spherical earth gravity and magnetic anomaly analysis by equivalent point source inversion. *Earth and Planetary Science Letters*, 53(1):69–83. doi:10.1016/0012-821x(81)90027-3.

Xia, J. and Sprowl, D. R. (1991). Correction of topographic distortion in gravity data. *GEOPHYSICS*, 56(4):537–541. doi:10.1190/1.1443070.

Xia, J., Sprowl, D. R., and Adkins-Heljeson, D. (1993). Correction of topographic distortions in potential-field data: A fast and accurate approach. *GEOPHYSICS*, 58(4):515–523. doi:10.1190/1.1443434.

ZhiWen, Z., ShuiYuan, H., XiaoHong, M., Jun, W., Yuan, F., ShiJing, Z., and KaiXun, L. (2022). Stable downward continuation of potential field data using an equivalent source method and a constrained strategy. doi:10.6038/cjg2022P0121.